Quake-DFN: A Software for Simulating Sequences of Induced Earthquakes in a Discrete Fault Network

Kyungjae Im*[1] and Jean-Philippe Avouac[1]

ABSTRACT

We present an earthquake simulator, Quake-DFN, which allows simulating sequences of earthquakes in a 3D discrete fault network governed by rate and state friction. The simulator is quasi-dynamic, with inertial effects being approximated by radiation damping and a lumped mass. The lumped mass term allows for accounting for inertial overshoot and, in addition, makes the computation more effective. Quake-DFN is compared against three publicly available simulation results: (1) the rupture of a planar fault with uniform prestress (SEAS BP5-QD), (2) the propagation of a rupture across a stepover separating two parallel planar faults (RSQSim and FaultMod), and (3) a branch fault system with a secondary fault splaying from a main fault (FaultMod). Examples of injection-induced earthquake simulations are shown for three different fault geometries: (1) a planar fault with a wide range of initial stresses, (2) a branching fault system with varying fault angles and principal stress orientations, and (3) a fault network similar to the one that was activated during the 2011 Prague, Oklahoma, earthquake sequence. The simulations produce realistic earthquake sequences. The time and magnitude of the induced earthquakes observed in these simulations depend on the difference between the initial friction and the residual friction $\mu_i - \mu_f$, the value of which quantifies the potential for runaway ruptures (ruptures that can extend beyond the zone of stress perturbation due to the injection). The discrete fault simulations show that our simulator correctly accounts for the effect of fault geometry and regional stress tensor orientation and shape. These examples show that Quake-DFN can be used to simulate earthquake sequences and, most importantly, magnitudes, possibly induced or triggered by a fluid injection near a known fault system.

KEY POINTS

- Quake-DFN is an efficient earthquake simulator applicable to complex discrete fault systems.
- Three comparison studies are conducted against publicly available simulation results.
- Induced earthquake simulations show realistic earthquake sequences corresponding to local stress fields.

Supplemental Material

INTRODUCTION

Much progress has been made recently in stress-based induced earthquake forecasting both at the conceptual level and in the modeling of real-case examples (e.g., McGarr, 2014; Segall and Lu, 2015; Langenbruch and Zoback, 2016; Bourne and Oates, 2017; Galis *et al.*, 2017; Goebel and Brodsky, 2018; Norbeck and Rubinstein, 2018; Zhai *et al.*, 2020; Hager *et al.*, 2021; Candela *et al.*, 2022; Wang and Dunham, 2022; Acosta *et al.*, 2023). The use of stress-based earthquake simulations to forecast-induced earthquakes, which account for known faults, remains, however, very challenging. Well-established methods exist to simulate individual dynamic rupture events on fault systems with complex geometries (e.g., Harris *et al.*, 2018) or to simulate repeating ruptures on faults with planar geometries (e.g., Erickson *et al.*, 2020; Jiang *et al.*, 2022). Combining the two capabilities is a computational challenge: resolving the effect of nonplanar fault geometries and the different phases of the earthquake cycle (the successive phases of nucleation, growth, and arrest of seismic ruptures).

There is, therefore, a need for computationally efficient earthquake simulators able to simulate earthquake sequences with

---

[1] Geology and Planetary Science Division, California Institute of Technology, Pasadena, California, U.S.A., https://orcid.org/0000-0003-0057-3119 (KI); https://orcid.org/0000-0002-3060-8442 (J-PA)

*Corresponding author: kjim@caltech.edu

Cite this article as Im, K., and J.-P. Avouac (2024). Quake-DFN: A Software for Simulating Sequences of Induced Earthquakes in a Discrete Fault Network, *Bull. Seismol. Soc. Am.* **XX**, 1–18, doi: 10.1785/0120230299

realistic fault geometries and loading. This need has motivated the development of RSQSim (Richards-Dinger and Dieterich, 2012). This simulator assumes that fault slip is governed by rate and state friction—a phenomenological friction law derived from laboratory experiments that allow simulation of the healing process during the interseismic period as well as the nucleation process and weakening (friction drop) during slip events. It allows the production of repeated ruptures on the same fault patch, accounting for effective stress changes induced by fluid injections (Dieterich *et al.*, 2015). RSQSim has been shown to produce synthetic catalogs with realistic statistical properties (Shaw *et al.*, 2018). The dynamics of seismic ruptures are, however, highly simplified by making use of a quasi-dynamic approximation with some additional kinematic prescriptions. The recently released simulator MCQSim (Zielke and Mai, 2023) adopted an alternative approach to represent dynamic effects during seismic ruptures. It assumes a linear decrease of friction with fault slip—a phenomenological law that can produce realistic seismic ruptures (e.g., Olsen *et al.*, 1997). This simulator produces realistic seismic ruptures, but the representation of healing and nucleation is simplified (not derived from solving the equations describing fault dynamics).

Here, we present an earthquake simulator, Quake-DFN, which is open source and allows computationally efficient simulations of sequences of induced earthquakes on a discrete fault network. We intend to produce realistic sequences of induced earthquakes consistent with the empirical statistical properties of earthquakes. Like RSQSim, our simulator assumes faults governed by rate and state friction embedded in a 3D half-space, driven by stress change that can result from tectonics or human activities such as the injection or extraction of fluids from the subsurface. We opt for a simplified representation of dynamic effects by adopting a quasi-dynamic approximation, but our formulation allows for inertial overshoot. This formulation is identical to the 2D discrete fault network simulator presented in Im and Avouac (2023), which was found to successfully reproduce the natural characteristics of earthquake sequences (Omori law, inverse Omori law, Gutenberg–Richter law). The representation of fault friction and the coupled processes involved in induced seismicity is oversimplified. In particular, we ignore that deformation affects fluid transport properties (e.g., Im *et al.*, 2018; Viesca and Garagash, 2018; Cappa *et al.*, 2022), but we believe that this simulator will be a useful tool to improve further the understanding of induced earthquakes and the management of the seismic hazard associated to CO_2 subsurface storage, geothermal energy production, or wastewater disposal (e.g., Zoback and Gorelick, 2012; Ellsworth, 2013; Candela *et al.*, 2018; Lee *et al.*, 2019).

Hereafter, we first describe the Quake-DFN simulation method and conduct comparison studies against publicly available simulation results. To illustrate the capabilities of the simulator, we describe sets of simulations with increasingly complex fault geometries. We start with a simple case of an injection of fluids in a pre-existing planar fault—a case also treated in several previous theoretical or numerical studies (e.g., Garagash and Germanovich, 2012; Dieterich *et al.*, 2015; Larochelle *et al.*, 2021; Bhattacharya and Viesca, 2019; Wang and Dunham, 2022; Sáez and Lecampion, 2023). We next consider the case of branching faults in the simple case of one single branch. We vary the orientation of the regional stresses and the angle between the fault branch and the main fault. Finally, we consider the case of the fault system activated during the 2011 Prague, Oklahoma, earthquake (Keranen *et al.*, 2013; Sumy *et al.*, 2014). We consider only the case of strike-slip faults here, but the simulator can apply to dip-slip faults.

SIMULATION METHOD

Simulation of fault slip with rate and state friction

Simulations of earthquake ruptures on finite-size faults governed by rate-and-state friction can yield realistic simulations of fluid-induced ruptures (e.g., Dieterich *et al.*, 2015; Cappa *et al.*, 2019; Hager *et al.*, 2021; Larochelle *et al.*, 2021; Wang and Dunham, 2022). Simulations based on rate and state friction are, however, computationally expensive and often associated with numerical instability. Stringent simplifications are therefore made in such simulations. Most assume a single planar fault with constant normal stress, neglecting off-fault deformation and the coupling between deformation and hydraulic properties (Dieterich *et al.*, 2015; Cappa *et al.*, 2019; Larochelle *et al.*, 2021). Even with these simplifications, simulating a sequence of earthquakes on a set of interacting faults is a huge challenge. RSQSim allows simulating sequences of earthquakes on a discrete set of faults by considering different stages (called “states” in the RSQSim literature; we use “stages” instead to avoid confusion) to solve the governing equations (Richards-Dinger and Dieterich, 2012; Dieterich *et al.*, 2015). The faults are discretized in planar cells and have a prescribed rake. In the period between rupture events, analytical approximations for noninteracting faults are used to solve for slip in stages 0 (healing) and 1 (nucleation). The nucleation process occurs within one cell, and the numerical scheme is, therefore, inherently discrete. During a rupture event (stage 2), the slip rate is prescribed and constant based on some chosen stress drop ($V^{\mathrm{EQ}} = 2\beta\Delta\tau/G$, in which β, $\Delta\tau$, and G are the shear-wave speed, stress drop, and shear modulus, respectively). The rupture velocity is then a consequence of this relationship.

In Quake-DFN, each fault is also discretized into rectangular planar cells, with a prescribed rake, in a 3D elastic half-space with quasi-static stress transfer. The main differences with RSQSim are that (1) Quake-DFN does not involve stage-based approximations nor kinematic prescriptions (the same set of governing equations is solved at all times), (2) the inherently discrete scheme is not needed (faults interact all the time and the cell size can be smaller than the nucleation size), and (3) inertial effects are represented with a lumped mass term (Im and Avouac, 2021b) in addition to the radiation damping term, introduced by Rice (1993), which is commonly used in quasi-dynamic simulations.

With these assumptions, the momentum balance equation at ith boundary element yields

$$M_i\ddot{\delta}_i = \sum_j k^{\tau}_{ij}(\delta_{0j} - \delta_j) - \mu_i\left(\sigma'_{0i} + \sum_j k^{\sigma}_{ij}\delta_j + \sigma'^{E}_i\right) - \frac{G}{2\beta}\dot{\delta}_i + \tau^E_i, \tag{1}$$

in which δ_i is the fault slip of element i, the over-dot denotes the time derivative, M_i is the lumped mass per unit contact area for each element, δ_{0j} is the initial displacement of element j,σ'_{0i} is the initial effective normal stress of element i, G is shear modulus, β is shear-wave speed, and k_{ij} is a stiffness matrix that defines the elastic stress change imparted on element i due to slip of element j (k^{τ} and k^{σ} represent shear and normal stiffness matrix, respectively). The stiffness matrices are calculated by assuming quasi-static stress transfer (Okada, 1992). The τ^E and σ'^E are shear and effective normal stress changes driven by external stress, such as tectonic loading or poroelastic stress change. To simplify notations, $V(=\dot{\delta})$ denotes fault slip velocity hereafter.

Faults are governed by rate and state friction (Dieterich, 1979; Marone, 1998),

$$\mu = \mu_0 + a\log\left(\frac{V}{V_0}\right) + b\log\left(\frac{V_0\theta}{D_c}\right), \tag{2}$$

and the aging law with the normal stress-dependent evolution (Linker and Dieterich, 1992),

$$\frac{d\theta}{dt} = 1 - \frac{V\theta}{D_c} - \alpha\frac{\theta\dot{\sigma}}{b\sigma}, \tag{3}$$

in which V is the slip rate, θ is the state variable, μ_0 is the friction coefficient at the reference velocity V_0 (chosen arbitrarily; here, we choose a value of 10^{-9} m/s), D_c is a critical slip distance, and a and b are empirical constants for the magnitude of direct and evolution effects, respectively. The Linker–Dieterich term, α, describes the effect of the normal stress rate on state evolution. It implies that the coefficient of friction is sensitive to normal stress evolution. It, therefore, comes into play when there is a significant change in normal stress (Alghannam and Juanes, 2020; Kroll *et al.*, 2023). The effect of pore pressure on fault slip is, however, primarily due to the impact on the effective stress, which occurs even if α is set to zero. For simplicity, we set $\alpha = 0$ for the simulations presented in the main text simulations. However, the influence of this term is presented in additional simulations and discussed in the supplemental material. We conducted multiple simulations with varied α values and found that this term plays an important role when α is sufficiently large ($\alpha > 0.12$). The state variable θ has a unit of time (s) and allows for frictional healing. Given $\alpha = 0$ in the main text simulations, the healing rate is maximum when the fault is stationary ($V = 0$). In that case, θ increases to 1 s/s (i.e., $d\theta/dt = 1$).

The radiation damping term, $\dot{\delta}_i G/2\beta$ (Rice, 1993) accounts approximately for the loss of energy due to seismic wave radiations. The lumped mass ($M_i\ddot{\delta}_i$) allows for inertial overshoot and friction-induced vibrations (Im and Avouac, 2021b). Overshoot appears in fully dynamic simulations and results in static slip larger than the slip that would have occurred in the absence of inertia (e.g., Madariaga, 1976; Thomas *et al.*, 2014). An overshoot factor, as defined by Ben-Zion (1996), is also included in RSQSim (Richards-Dinger and Dieterich, 2012) or MCQSim (Zielke and Mai, 2023). The lumped mass per unit area M represents the inertia of the mass involved in the rupture process. If the rupture size is fixed and assumed to be equal to the fault size, M can be defined as

$$M = \frac{\rho L}{(1-\nu)\pi^2}, \tag{4}$$

in which L is the length scale of the rupture size, ρ is rock density, and ν is Poisson's ratio. Conversely, if the rupture size is not fixed, L may be approximated by the expected rupture scale in the simulations. In this work, we assumed a constant M value of 10^6 kg/m^2 for the planar fault simulation and 10^7 kg/m^2 for the other simulations. If $M = 0$, equation (1) is simplified to the widely used quasi-dynamic approximation (Rice, 1993; Lapusta *et al.*, 2000; Erickson *et al.*, 2020). We show later that our simulation results become equivalent to those obtained in quasi-dynamic simulations if M is sufficiently small. The simulation uses the method of Im *et al.* (2017), which allows larger timesteps during the rupture phase using the lumped mass term. Therefore, in Quake-DFN, the lumped mass term helps stabilize the numerical scheme and accelerate numerical convergence. One needs to keep in mind that the dynamic stress transfers associated with seismic waves are not resolved, so Quake-DFN cannot estimate the rupture velocity, but it can correctly predict slip distributions as happens in quasi-dynamic simulations (Thomas *et al.*, 2014). Our simulator has no restriction on grid size. But to avoid an inherently discrete scheme, one may choose a grid size smaller than the critical length scale (Rice, 1993),

$$L_c = \frac{\gamma G D_c}{\sigma(b-a)}, \tag{5}$$

in which γ is a factor close to unity, which depends on the shape of the grid cells.

Three different fault geometries are considered in the simulations presented in this study: (1) a single planar fault (Fig. 1a), (2) two interacting discrete faults (Fig. 1b), and (3) a complex fault network adopted from studies of the 2012 Prague, Oklahoma, earthquake sequence (Keranen *et al.*, 2013; Sumy *et al.*, 2014; Fig. 1c). In the planar fault

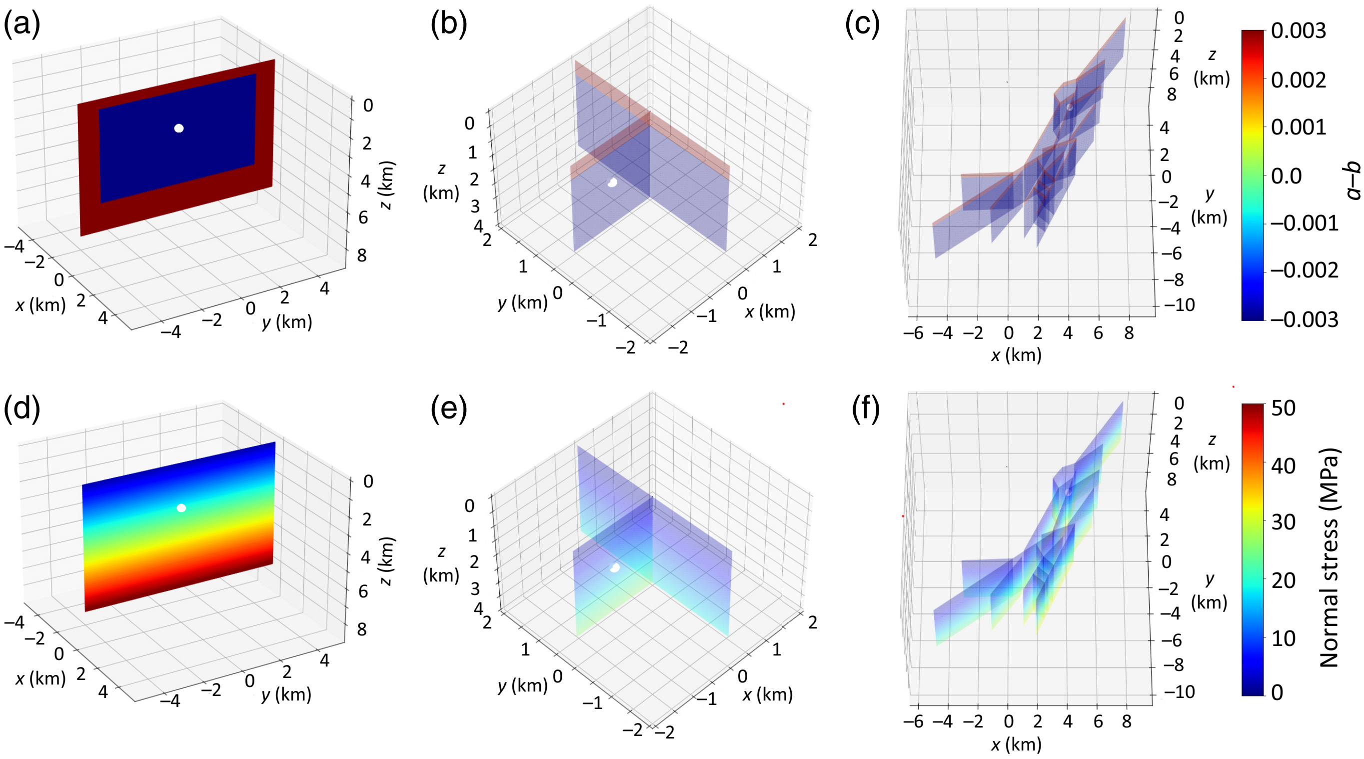

Figure 1. Fault geometries with distributions of (a–c) friction parameters $a - b$ and (d–f) normal stress are considered in the simulations of injection-induced seismicity presented in this study. The white sphere denotes the injection location. (a,d) Single vertical planar fault. (b,e) Branching faults for a 90° angle and simulations for a 60° angle were also conducted. (c,f) A complex fault system with geometry adopted from the 2012 Prague, Oklahoma, earthquake. The normal stress is assumed to increase linearly with depth. Different values of the stress gradient were also tested. The color version of this figure is available only in the electronic edition.

simulations, we investigate the influence of the initial conditions of V_i and θ_i. In the other two cases, the initial friction μ_i is calculated from the applied stress field, θ_i is assumed to be in the range of years to tens of thousand years, and V_i is determined accordingly based on equation (2).

Given the bulk medium properties (M, G, β, k_{ij}) and the fault friction parameters (a, b, D_c, μ_0), the set of equations (1)–(3) can be solved for any initial conditions represented by μ_i, V_i, and θ_i. The initial friction coefficient (μ_i) is determined by the local stress tensor. Hence, the only two values that are typically unknown are the initial values of the velocity (V_i) and state variable (θ_i). We can bracket the initial value of θ_i because its maximum value is the elapsed time from the last rupture (maximum $d\theta/dt = 1$ s/s), whereas V_i has no such limit. For example, in the Prague earthquake simulation, we first set the initial θ_i in the range between 10^{10} and 10^{12} s (300–30,000 yr), and V_i is determined correspondingly by equation (2).

We use two methods to solve equations (1)–(3): (1) a typical iterative method that is applied to a low-velocity system and (2) the method of Im *et al.* (2017), which is stable at high velocity. The two solvers are automatically switched for each element based on their velocities. The timestep is dependent on the maximum velocity but automatically adapts if it fails to find a converged solution.

Simulation of pore pressure diffusion and poroelastic stress transfers

The external shear and effective normal stress terms, respectively, τ^E and σ'^E in equation (1), are time-dependent and can account for tectonic loading or porothermoelastic stress changes. These forcing terms can be calculated from an external geomechanical model. In the simulations of injection-induced seismicity presented in this study, we follow the approach of Segall and Lu (2015). We calculate poroelastic stress change assuming isotropic pressure diffusion from a point source of injection. The governing equation for pressure diffusion is

$$\frac{k}{\eta}\nabla^2 P + q = S\frac{\partial P}{\partial t}, \qquad (6)$$

in which P is pressure, k is permeability, η is viscosity, q is volumetric flow rate, and S is storage coefficient. The spherical diffusion solution of equation (6) and the corresponding poroelastic stress change are given by Rudnicki (1986). The solutions are evaluated at the center of each element and rotated for each fault plane and slip direction to estimate τ^E and σ'^E. We use constant viscosity ($\eta = 0.4 \times 10^{-3}$ Pa/s), density (1000 kg/m^3), and storage ($S = 2 \times 10^{-11}$; S is equivalent

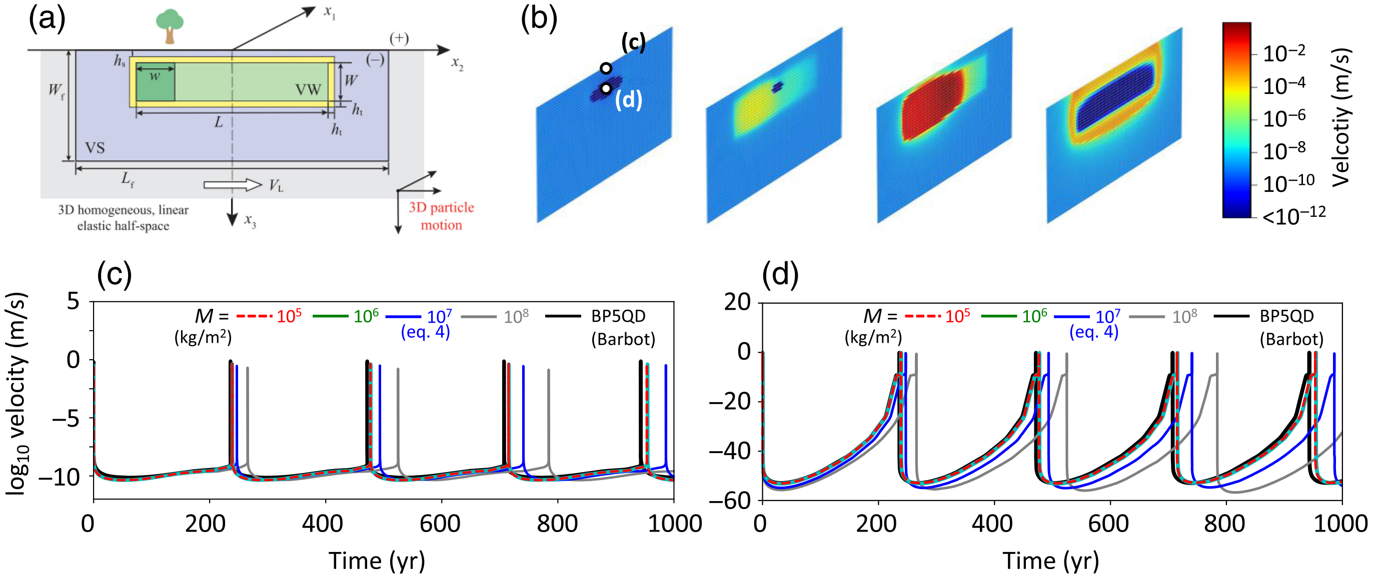

Figure 2. Comparison study 1, planar fault. (a) Setup of the SEAS project benchmark test BP5-QD (Jiang *et al.*, 2022). (b) Snapshots of slip rate distribution in our simulation for $M = 10^5$ kg/m^2. (c,d) Evolution of the slip rate at two points (see panel (b), for their location) for comparison of the benchmark simulation (red dashed line) with our simulation result (with $M = 10^5$ (red dashed), 10^6 (green), 10^7 (blue), and 10^8 kg/m^2 (gray). We selected the benchmark simulation run with Unicycle (Barbot, 2019; black line), which is available on the SEAS project website. The red dashed and green lines are completely overlapping. The color version of this figure is available only in the electronic edition.

to $k/\eta c$ in Rudnicki's solution) for all simulations. This model was chosen for simplicity. In reality, the permeability would be neither homogeneous nor isotropic, and faults and fractures usually have greater permeability than the rock matrices. The pressure sometimes becomes higher than the initial normal stress, leading to numerical instability. To avoid such instability, we impose the minimum effective normal of 2 MPa.

COMPARISON STUDIES

Here, we compare our simulator to publicly available simulation results. These tests are meant to show that Quake-DFN adequately simulates seismic ruptures for simple fault geometries in the absence of any fluid injection. We conducted simulations of three standard problems: (1) the rupture of a planar fault with uniform prestress, (2) the propagation of a rupture across a stepover separating two parallel planar faults, and (3) a branch fault system with a secondary fault splaying from a main fault.

Comparison study 1: Planar fault (SEAS BP5-QD benchmark test)

We tested our simulator in the case of a simple planar fault geometry against the benchmark problem—BP5QD (quasi-dynamic planar fault rupture simulation) from the Community Code Verification Exercise for Simulating Sequences of Earthquakes and Aseismic of the Southern California Earthquake Center (Erickson *et al.*, 2020; Jiang *et al.*, 2022). This test allows checking that our simulator is consistent with the widely used quasi-dynamic formulation when the lumped mass term is small. Given the average length scale of rupture zone size of the BP5QD problem is 36 km (60 km × 12 km), according to equation (4) with $\rho = 2670$ kg, the lumped mass $M = \sim 10^7$ kg/m^2. We conducted four simulations with $M = 10^5, 10^6, 10^7$, and 10^8 kg/m^2. This sensitivity test is to investigate the influence of the M on the inertial overshoot. As M decreases, the simulation result should converge to benchmark results because equation (1) approaches the widely used quasi-dynamic formulation.

Our simulation compares well with the SEAS benchmark test (Fig. 2). The simulation with the nominal mass (given by equation 4) shows a slightly longer recurrence time and larger stress drop (blue line) than the benchmark solution (black line) due to the inertial overshoot. The overshoot effect increases if we increase M (gray line). Conversely, as expected, the simulation result converges to the benchmark simulation result as we reduce M. When the effect of the mass is not negligible, overshoot results in a larger slip and stress drop than for a quasi-dynamic slip event. As a result, the time interval between successive events has increased. This benchmark test shows that our simulation results are consistent with the quasi-dynamic formulation, as the inertial overshoot effect vanishes.

Comparison study 2: Fault stepover

The second comparison test is a stepover fault system (Fig. 3a). It consists of two parallel planar left-lateral faults, in which a rupture can jump from one fault to the other across a compressional stepover. The two faults have the same uniform initial stress. Simulations of this comparison test conducted with

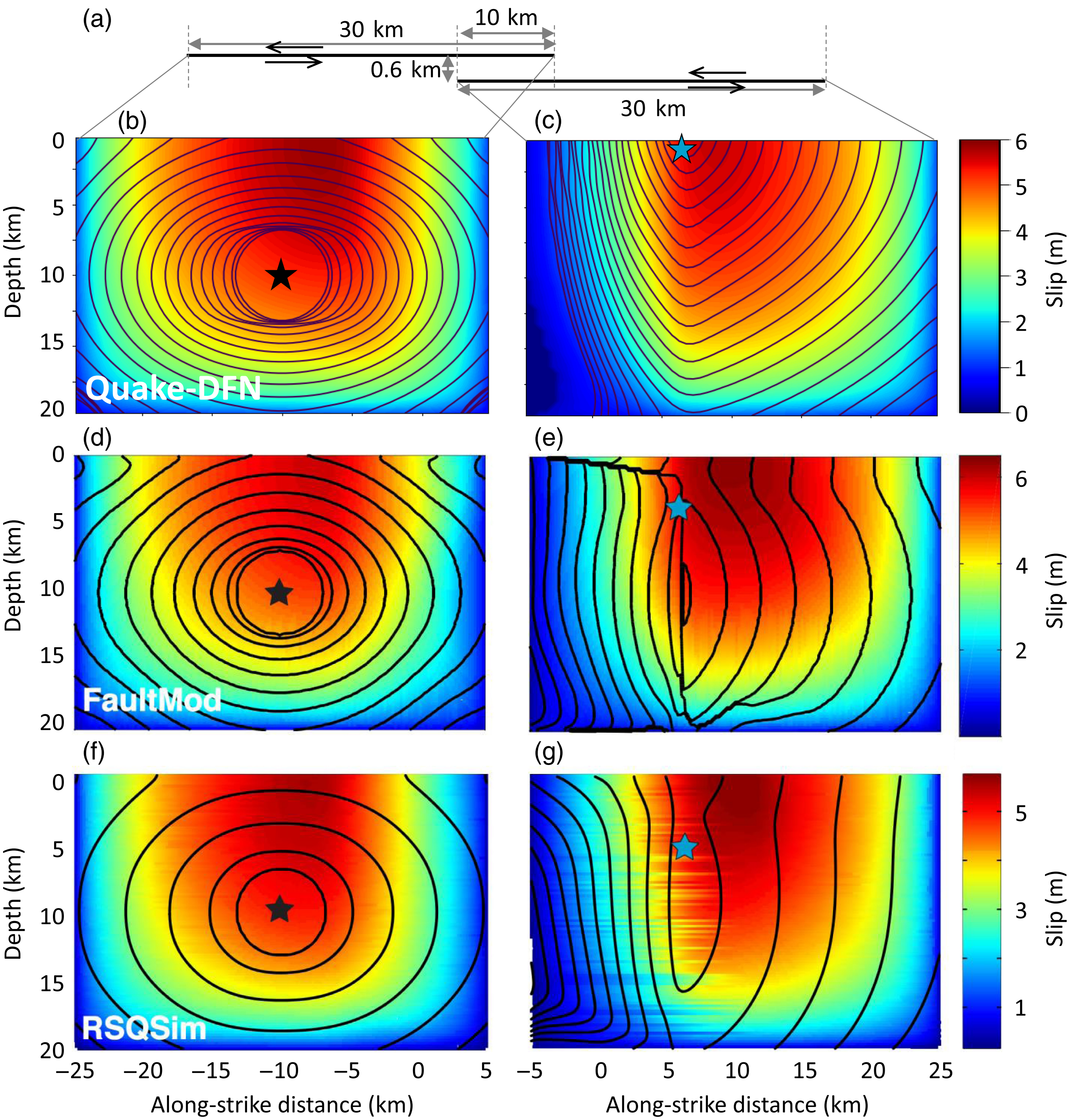

RSQSim and FaultMod are presented in Kroll *et al.* (2023). These simulators solve the friction-governed motion of fault slip, but their governing equations differ from our simulator. FaultMod is a fully dynamic finite element solver with slip-weakening friction. RSQSim is, like Quake-DFN, a boundary element solver based on rate and state friction with quasi-static stress transfer (Richards-Dinger and Dieterich, 2012). Instead of using radiation damping or a lumped mass, it resorts to a stage-based approximation with a constant dynamic slip rate (In Kroll *et al.*, 2023, the authors used the fault-slip rate

Figure 3. Comparison study 2, fault stepover. (a) Fault configuration. (b–g) Simulation results of (b,c) Quake-DFN, (d,e) FaultMod, and (f,g) RSQSim. The colored map denotes slip distribution at the end of the rupture sequence, and the black curves represent the rupture contour every 0.5 s. Rupture is forced to nucleate at the black star. The blue stars denote the nucleation point in the receiver fault. Panels (d)–(g) are adopted from Kroll *et al.* (2023). The color scales for these panels are slightly different. The color version of this figure is available only in the electronic edition.

prescribing a rupture velocity equal to that predicted by FaultMod). Hence, we do not expect Quake-DFN to yield results identical to those obtained with RSQSim or FaultMod by Kroll *et al.* (2023). In our Quake-DFN simulations, we pay attention to replicating the slip distribution (or, equivalently, the stress drop), because our aim is primarily to correctly predict the final magnitude. The rupture velocity and fault slip rates are probably not physical during seismic slip, given the way dynamic effects are approximated. However, the results obtained with FaultMod, RSQSim, and Quake-DFN should be comparable about the slip distributions. To replicate the problem as described in Kroll *et al.* (2023), the normal stress is set uniformly at 60 MPa on both faults. We impose friction parameters ($a = 0.01$, $b = 0.012$, $D_c = 10\ \mu\mathrm{m}$) and initial conditions ($\theta_i = 2.6 \times 10^{10}$ and $V_i = 2.17 \times 10^{-13}$) to simulate the friction drop described in Kroll *et al.* (2023) (initial friction 0.49 dropping to ~0.38).

Our simulation result is indeed comparable to the compared simulations. The final slip distribution is similar in all simulators (Fig. 3, colormap), except some horizontal spikes appear in RSQSim (Fig. 3f,g). Conversely, rupture propagation is somewhat different between the solvers. In our simulation, the rupture speed is slower, as has been found in previous studies comparing quasi-dynamic and fully dynamic solvers (e.g., Thomas *et al.*, 2014; Erickson *et al.*, 2023). Also, the location where the second rupture nucleates after jumping across the stepover is different (blue star in Fig. 3c,e,g). It is shallower in our simulation. This test shows that the rupture speed and nucleation behavior are indeed sensitive to the solution method and whether stress transfer is dynamic or quasi-static. Nevertheless, the distribution of slip is similar in all three simulations, showing that the final magnitude and stress drop distributions calculated with Quake-DFN are valid.

Comparison study 3: Fault branching

The last comparison study considers a branching fault system. We compare our modeling with the solution obtained with FaultMod to the TPV18 benchmark test of the Statewide California Earthquake Center (SCEC) and U.S. Geological Survey (USGS) Spontaneous Rupture Code Verification Project (Harris *et al.*, 2009, 2018). The TPV18 exercise solves a single-earthquake rupture with a 30° branch fault (Harris *et al.*, 2018). Again, because FaultMod is a fully dynamic solver with slip-weakening friction, it would not give a solution identical to our quasi-dynamic rate and state friction solution. However, the two solutions should be comparable when the parameters lead to a similar magnitude of friction drop. Following the TPV18 problem description, the initial stress tensor is depth-dependent, and the initial stress on the branch fault is lower than that on the main fault at the same depth (Fig. 4a). We set $a = 0.006$, $b = 0.013$, $D_c = 1$ mm, $\theta_i = 10^{10}$, and $V_i = 10^{-12}$ to achieve dynamic friction of ~0.12. This setup produces a similar magnitude of stress drop to the benchmark simulation (Fig. 4).

Our simulation result is again comparable to the FaultMod solution for the benchmark simulation. The evolution of stress and slip predicted by FaultMod at a selection of points is provided on the website of the SCEC/USGS Spontaneous Rupture Code Verification Project (Fig. 5b). We calculated the displacement and stress evolution at those points and found them very similar to those obtained with FaultMod (Fig. 5). The fault slip decreases near the surface (Fig. 5a) because the stress drop is insignificant there due to the low initial stress. One significant difference is that the shallow rupture initiates earlier in our simulation (blue solid lines) than in the FaultMod solution (blue-dashed line). This is presumably due to the quasi-static stress transfer, which immediately changes stresses everywhere.

INJECTION-INDUCED EARTHQUAKES ON A PLANAR FAULT

In this set of simulations, we investigate the effect of an injection into a planar fault. This problem has also been treated in several previous studies (Garagash and Germanovich, 2012; Galis *et al.*, 2017; Larochelle *et al.*, 2021; Sáez and Lecampion, 2024). They showed that, depending on the initial stress, rupture might either be "self-arrested," meaning that it is confined to the area of increased pore pressure or might run away outside of it. The runaway rupture can occur when the dynamic friction (μ_d, the friction at the end of the rupture) is smaller than the initial friction μ_i, that is, $\mu_i - \mu_d > 0$ (Garagash and Germanovich, 2012). The dynamic friction μ_d can be approximated in rate and state formulation as steady-state residual friction at the rupture peak slip rate (V_P): $\mu_f = \mu_0 + (a - b) \log(V_P/V_0)$ (Larochelle *et al.*, 2021). One may approximate the rupture peak slip speed $V_P = 1$ m/s, and then the runway potential can be defined as

$$\mu_i - \mu_f = \mu_i - \mu_0 + (a - b)\log(V_0), \tag{7}$$

or equivalently from equation (2):

$$\mu_i - \mu_f = a\log(V_i) + b\log\left(\frac{\theta_i}{D_c}\right). \tag{8}$$

The approximated condition for runaway rupture is $\mu_i - \mu_f > 0$. Equations (7) and (8) imply that, in terms of the model parameters and initial conditions, the rupture magnitude should be primarily dependent on $\mu_i - \mu_0$ (equation 7), hence on the initial values of V_i and θ_i (equation 8).

We consider a 10 × 7 km vertical planar fault with an 8 × 5 km unstable fault patch (Fig. 1a). Unstable fault has $a = 0.003$ and $b = 0.006$. The fault area around that patch is rate-strengthening, with $a = 0.006$ and $b = 0.003$. D_c is set to 200 μm everywhere. The normal stress gradient is 7 kPa/m (Fig. 1d). The element size is 50 m for the unstable zone and 100 m for the stable zone. A lumped mass

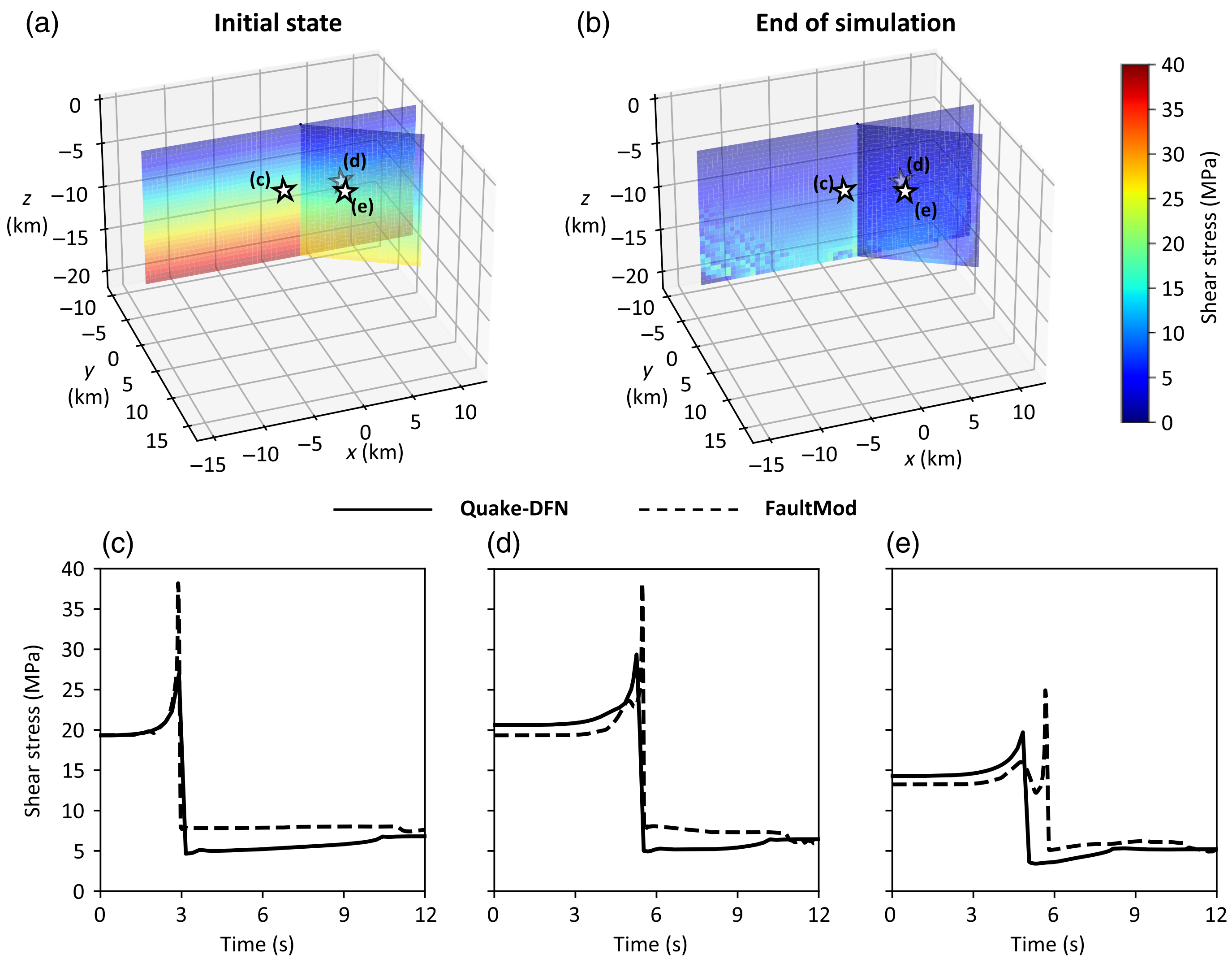

Figure 4. Comparison study 3, stress changes. (a) Initial and (b) final shear stress. Initial stress is depth-dependent for both faults, with the branch fault having lower initial stress. (c–e) Shear stress versus time at each location is denoted in panels (a) and (b). The time of the Quake-DFN result is shifted by 453 s due to the longer nucleation time—a feature that results from assuming rate and state friction in Quake-DFN instead of slip-weakening friction in Fault Mod. The color version of this figure is available only in the electronic edition.

$M = 10^6\ \mathrm{kg/m^2}$ is assigned to each element. The injector is located at 2.5 km depth with a flow rate of $0.1\ \mathrm{m^3/s}$ (100 kg/s) and a permeability of $10^{-16}\ \mathrm{m^2}$. We conducted three simulations with constant $\mu_0 = 0.3$ and different initial conditions going from less to more critical: (1) $V_i = 10^{-30}$ and $\theta_i = 10^6$, (2) $V_i = 10^{-20}$ and $\theta_i = 10^3$, and (3) $V_i = 10^{-15}$ and $\theta_i = 10^9$. According to equation (8), $\mu_i - \mu_f$ of each case is (1) −0.073, (2) −0.046, and (3) 0.072, implying that only the third case has a high potential for runaway rupture since $\mu_i - \mu_f > 0$.

As found in previous studies, our simulations show self-arrested and runaway ruptures. The self-arrested rupture occurs when $\mu_i - \mu_f < 0$ (low V_i and θ_i; Fig. 6a–h). In this regime, the magnitudes of the induced earthquake increase with time (and with injection volume because the injection rate is constant). The earthquake is smaller in the early stage (Fig. 6a,e) and grows larger in the later stage (Fig. 6b,f). Conversely, when $\mu_i - \mu_f > 0$ (high V_i and θ_i; Fig. 6i–l), runaway rupture occurs at the very early stage (Fig. 6i). The fault runaway potential resets after the initial runaway rupture, and a self-arrested rupture occurs within the unstable zone (Fig. 6j).

In the self-arrested rupture sequences, the induced earthquakes nucleate near the injector and migrate away with time (Fig. 6d,h). Most of the large events are nucleated slightly away (>500 m) but not too far (<2000 m) from the injector. This is likely because the high pressure near the injector stabilizes fault slip in the rate and state framework (according to equation 5), as observed in previous simulations and in situ experiments (Guglielmi *et al.*, 2015; Bhattacharya and Viesca, 2019; Cappa *et al.*, 2019; Larochelle *et al.*, 2021). These simulations show the potential of our simulator to gain insight into the factors controlling the timing and magnitudes of sequences of induced earthquakes in the particular simple case of a single planar fault.

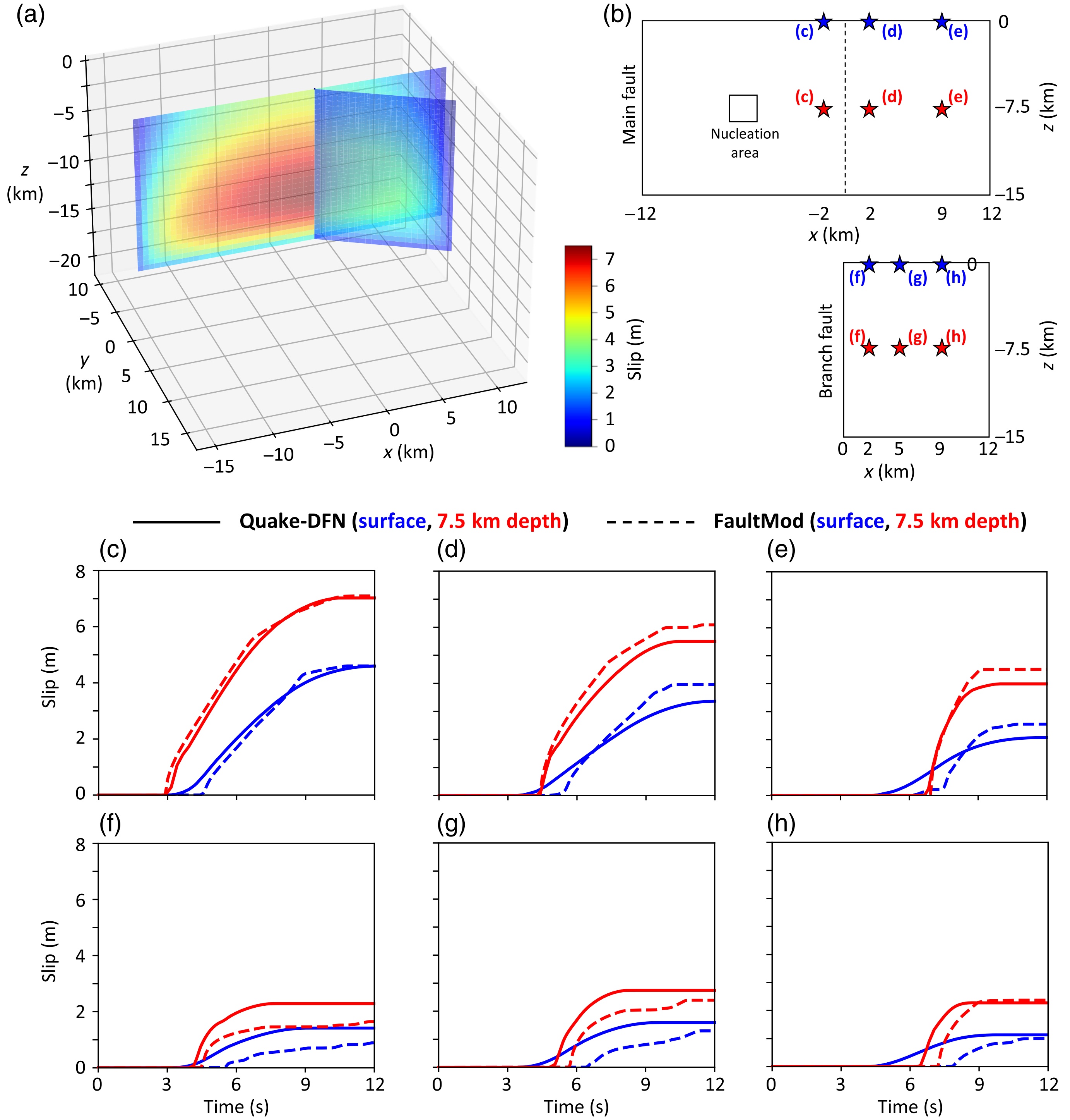

Figure 5. Comparison study 3, fault slip. (a) Map of fault slips in our simulation result. (b) The location of the time plot is shown in panels (c)–(h). Fault slip versus time for each location indicated in panel (b). Solid and dashed lines denote our simulation result and the FaultMod simulation result, respectively. The time of the Quake-DFN result is shifted by 453 s due to the longer nucleation time. The color version of this figure is available only in the electronic edition.

INJECTION-INDUCED EARTHQUAKES ON A BRANCHING FAULT SYSTEMS

We now move to a more complex setup in which fluid is injected into a secondary fault that is branching out from a larger fault (Figs. 1b and 7). Both the faults are assumed to be planar. This set of simulations was designed to show that our simulator can be used to explore how the branching fault geometry relative to the regional stress field affects induced seismicity. We consider two strike-slip faults at two different

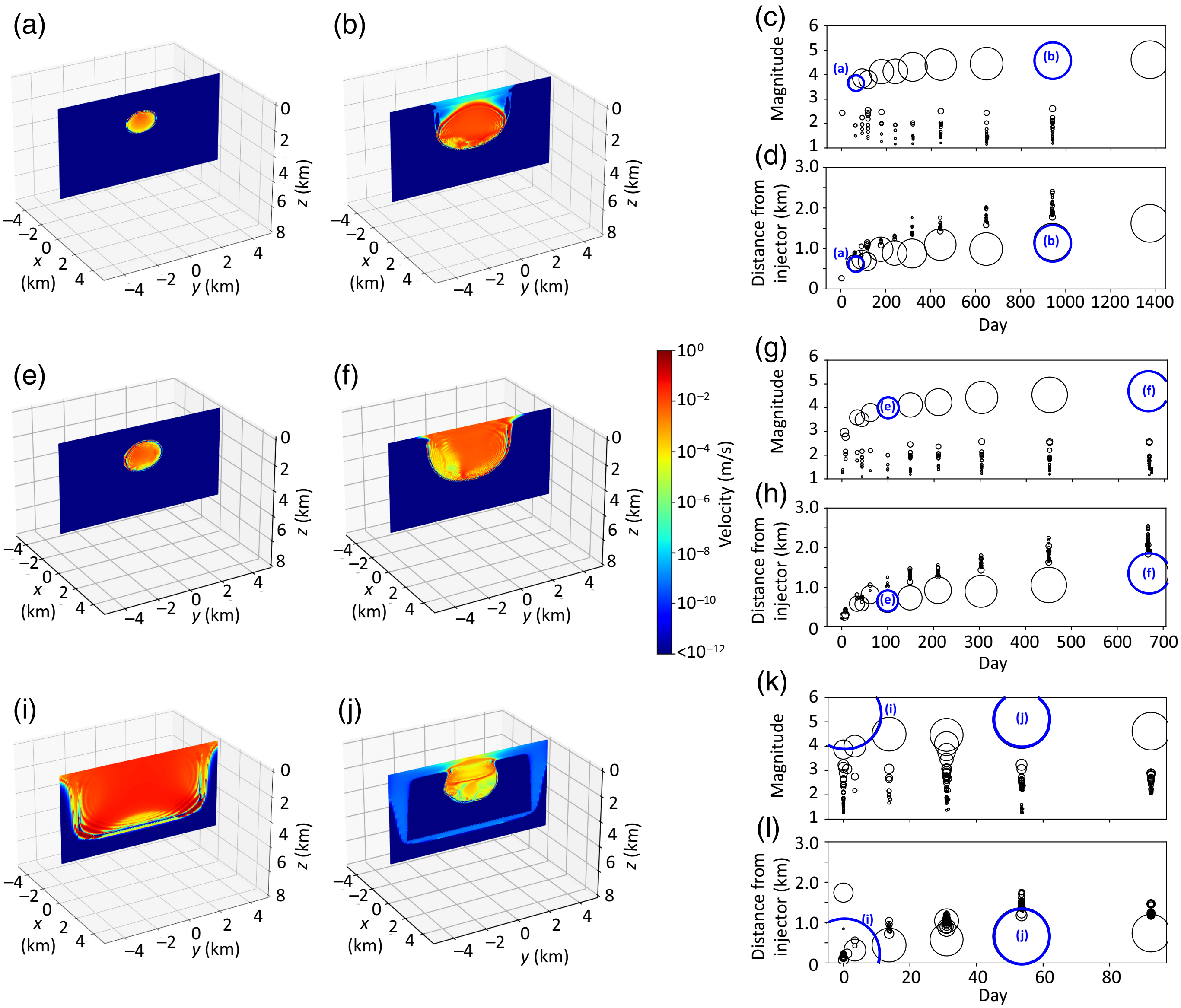

Figure 6. Simulation of earthquakes induced by a fluid injection into a planar fault. (a–d) Simulation result with $V_i = 10^{-30}$ and $\theta_i = 10^6$ s. (e–h) Simulation result with $V_i = 10^{-20}$ and $\theta_i = 10^3$ s. (i–l) Simulation results with $Vi = 10^{-15}$ and $\theta_i = 10^9$ s. (a,b,e,f,i,j) Snapshots of slip velocity during particular events. (c,g,k) Magnitude versus time. (d,h, l) Distance from the injector versus time. The events corresponding to each snapshot are labeled in the time series plot. The color version of this figure is available only in the electronic edition.

angles (90° and 60° in Fig. 7a and 7b, respectively). Both the faults are unstable ($a = 0.003$, $b = 0.006$, and $D_c = 200$ μm) but with a shallow stable zone at a depth less than 500 m ($a = 0.006$, $b = 0.003$, and $D_c = 200$ μm; Fig. 1b). Lumped mass $M = 10^7$ kg/m^2 is assigned to each element. One fault is longer (4 km × 3 km) than the other fault (2 km × 3 km). The element size is uniform and equal to 70 × 70 m. The injector is located at 1.5 km depth at the center of the shorter fault with a flow rate of 0.03 m^3/s (30 kg/s). We assume a permeability of 3×10^{-16} m^2 for all simulations. The simulations run for 50,000 timesteps, sufficiently covering a time duration of 1 yr.

We conducted simulations by varying the maximum stress orientation by increments of 15° (Fig. 7a,b, dashed lines). Maximum stress has a depth gradient of 10 kPa/m, and minimum stress is assumed to be 50% of the maximum. The initial stress and friction are determined based on the stress orientation and magnitude. The value of $\mu_i - \mu_f$, which defines the runaway potential, is determined by the maximum stress angle (that determines μ_i) and μ_0 (that determines μ_f, equation 7). To test the influence of $\mu_i - \mu_f$, we vary μ_0 between 0.32 and ~0.48. We assume a uniform initial state variable $\theta_i = 10^8$ s (3 yr), and the initial velocity V_i is determined based on equation (2). Since θ_i is constant, the potential for a runaway rupture is determined by V_i. If the faults are optimally oriented to the stress field, V_i is high (Fig. 7c). Conversely, if faults are nonoptimally oriented, V_i is low (Fig. 7d).

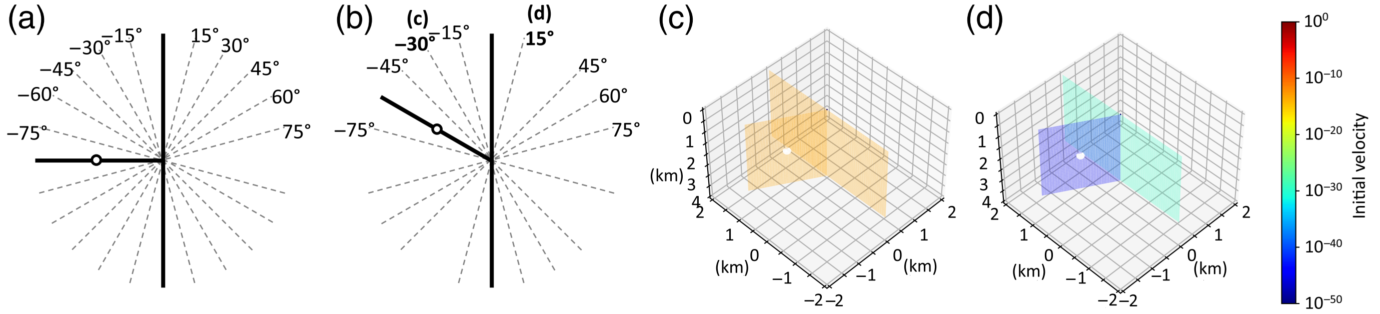

Figure 7. Simulation set up for two interacting faults. (a,b) Fault orientation (bold lines) and maximum stress orientation tested (dashed lines) for an angle between the two faults of (a) 90° and (b) 60°. White circles denote injector locations. (c,d) Initial velocities of fault angle 60° with $\mu_0 = 0.4$, $\theta_i = 10^8$ s and maximum stress (c) −30° and (d) 15° (angles shown in panel (b)). The color version of this figure is available only in the electronic edition.

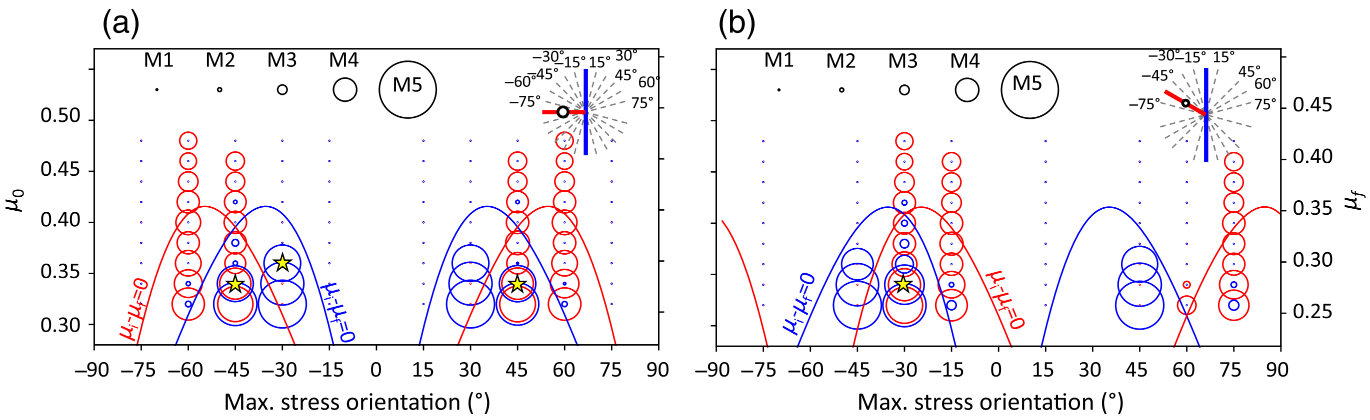

Figure 8. Maximum magnitude on the main fault (blue) and the branch fault (red) within one year for an angle between the two faults of (a) 90° and (b) 60°. The simulation setup (detailed in Fig. 7) and the location of the injection are recalled in the inset of each panel. Blue circles denote events on the main fault, and red circles denote events on the branch fault in which the injection takes place. The rupture sequences for selected cases (yellow stars) are shown in Figure 9. The moments are calculated separately for each fault, even in the case in which both faults are ruptured simultaneously. Red and blue curves denote the contour line of $\mu_i - \mu_f = 0$ for branch and main faults, respectively. The color version of this figure is available only in the electronic edition.

The two-fault simulations illustrate the effects of the initial stress field and faults interaction. We find that the rupture occurs in the one-year time window of the simulation if the fault is near optimally oriented (30° and 45° from maximum stress orientation; Fig. 8). The main fault (blue) ruptures only when the maximum stress angle is ±45 or ±30, and the branch fault (red) only ruptures when the maximum strike angle is ±60° or ±45° in Figure 8a and −30°, −15°, and 75° in Figure 8b. The main fault rupture is well predicted by runaway potential because it only ruptures when $\mu_i - \mu_f > 0$. The magnitude of the maximum event increases as μ_0 decreases (i.e., runaway potential increases). The results, together with the planar fault simulation results presented in the Injection-Induced Earthquakes on a Planar Fault section, show that the risk of an induced earthquake can be primarily determined by runaway potential $(\mu_i - \mu_f)$.

In all cases, the main fault (blue) ruptures only when μ_0 is low enough, whereas the branch fault (red) ruptures up to a much higher μ_0 value as long as the fault is near-optimally oriented. This is expected because the branch fault is submitted to larger poroelastic stresses than the main fault, which is farther away from the injection. The main fault is loaded mainly by slip on the branch fault, whether seismic or aseismic (i.e., faults interaction).

The interactions comply with the prescribed stress field. For instance, in the case of a maximum stress orientation of 45°, the slip on the branch fault is left lateral (Fig. 9a). It reduces normal stress on the north side of the main fault, causing the earthquake on the main fault to propagate toward the north first. The reverse happens in the case of a maximum stress orientation of −45°, in which the branch fault is right lateral and the main fault earthquake propagates toward the south first

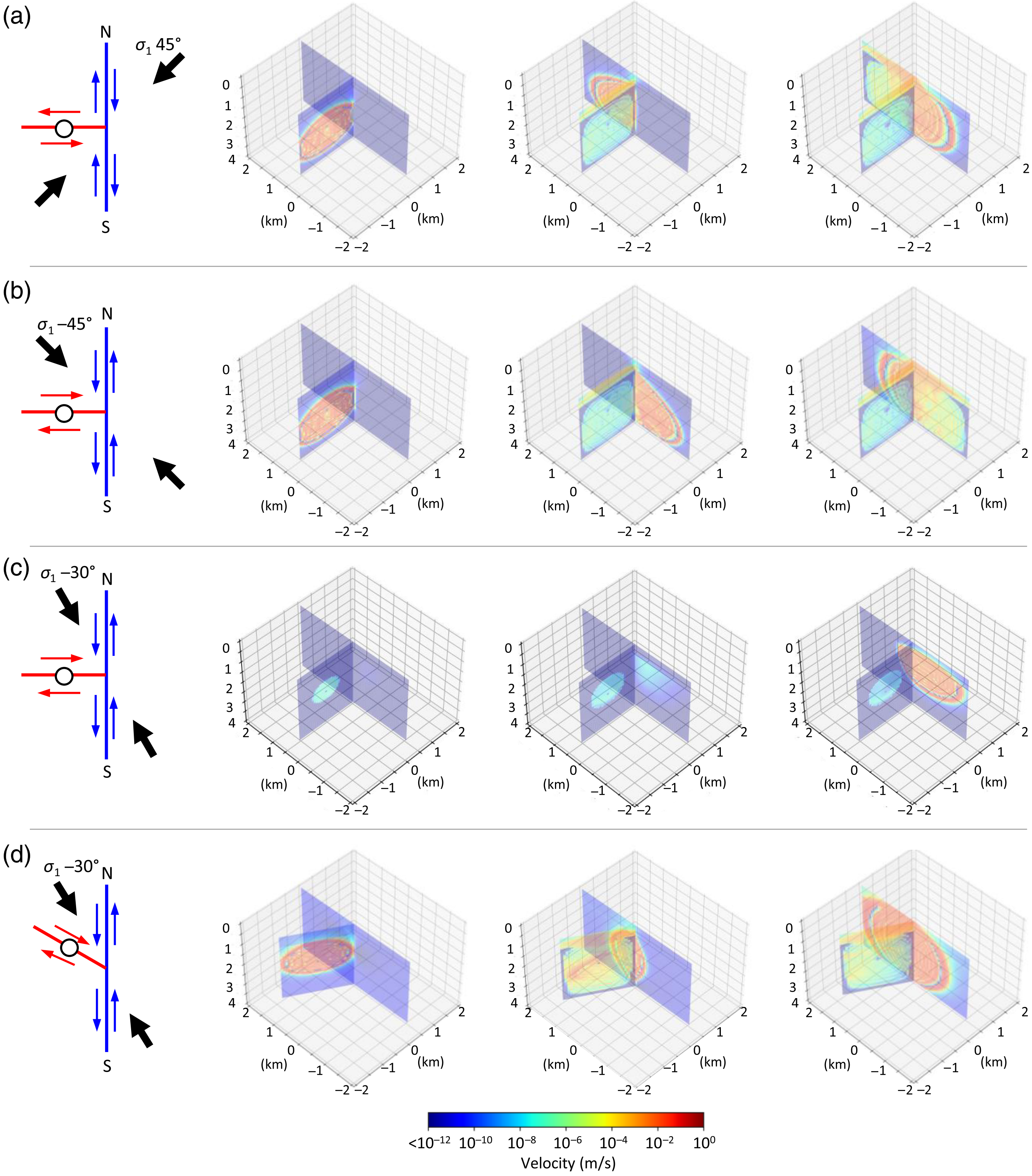

Figure 9. Snapshots of slip velocity during seismic ruptures induced by a fluid injection into a branch fault system. The fault geometry and maximum stress orientation of each panel (a)–(d) are shown on the left and in Figure 8 (yellow star). In all cases, slip is initiated on the branch fault (red) by the fluid injection, can be seismic or aseismic, and triggers a fault rupture on the main fault (blue). The color version of this figure is available only in the electronic edition.

(Fig. 9b). In the 60° angle fault geometry with a maximum stress orientation of −30°, the triggered rupture propagates both north and south (Fig. 9d). This is due to the normal stress effect competing with the shear stress effect. In the northern part of the Blue Fault, both the normal and shear stress are increased, and the opposite occurs in the southern part. Also, we find that an aseismic-to-seismic interaction can occur,

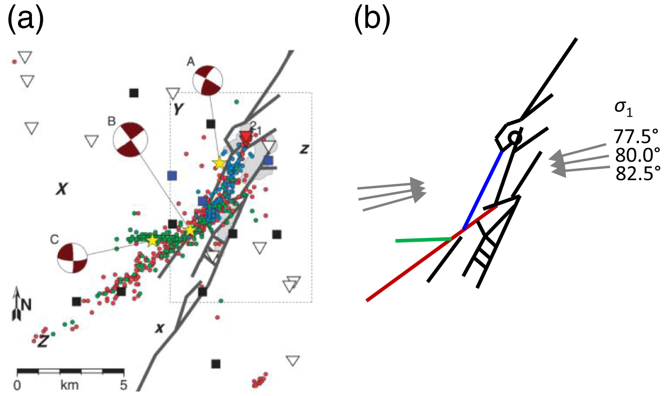

Figure 10. Fault geometry for Prague earthquake sequence simulation. (a) Wilzetta fault map used for reference with focal mechanisms of the M_w 5.0 foreshock (A), M_w 5.7 mainshock (B), and M_w 5.0 aftershock faults (C) (figure from Keranen *et al.*, 2013). (b) The fault map was used for the simulation. Blue, red, and green faults were activated by the M_w 5.0 foreshock, M_w 5.7 mainshock, and M_w 5.0 aftershock faults, respectively. The faults ruptured during the mainshock and aftershock faults were not mapped on the original map. Gray arrows denote the three maximum stress orientations tested in this work. The color version of this figure is available only in the electronic edition.

as observed in the Brawley geothermal field, where injection-induced aseismic slip on a shallow normal fault triggered a strike-slip earthquake on a deeper fault (Im and Avouac, 2021a). Aseismic slip on the nonoptimally oriented fault can trigger earthquakes in the other optimally oriented fault (Fig. 9c).

A REALISTIC CASE EXAMPLE: THE PRAGUE, OKLAHOMA, EARTHQUAKE SEQUENCE

The simulation is designed to approximate the geometry of the Wilzetta fault system, which ruptured during the 2011 Prague, Oklahoma, earthquake sequence (Keranen *et al.*, 2013; Sumy *et al.*, 2014). The sequence consists of a cascade of three larger events of magnitude M_w 5.0, 5.7, and 5.0, which occurred within 3 days. The injection began in 1993, and the flow rate was kept under 1500 $\mathrm{m}^3/month$ (~0.58 kg/s; Keranen *et al.*, 2013). No earthquake had been reported on that fault system until an M 4.1 event in February 2010. The Prague earthquake sequence occurred in November 2011.

The geometry and injection location (Fig. 10) are adopted from Keranen *et al.* (2013), with the addition of the faults ruptured by the 5.7 and 5.0, which had not been recognized before the earthquake sequence. The faults were discretized with an element size of 200 m. The simulation assumes a maximum stress (σ_1) orientation of ~N80°E (Sumy *et al.*, 2014). The point-source injector is located at a depth of 1500 m. We used a constant flow rate of 0.27 kg/s (~700 $\mathrm{m}^3/\mathrm{month}$), which is a rough average of the actual flow rate between 1993 and 2011 (Keranen *et al.*, 2013), with a permeability of 3×10^{-18} m^2.

For the sensitivity test, a total of 36 simulations were conducted: we tested two values of θ_i (300 yr, 30,000 yr), three values of σ_1 orientations (75°, 80°, 85°N; Fig. 10b), and six values of μ_0 for each of the stress setups. The minimum stress is set as half of the maximum stress, $\sigma_3/\sigma_1 = 0.5$, because we found by trial and error that this ratio best reproduces the observed earthquake sequence. The range of μ_0 is determined to cover both mainshock ruptured and unruptured scenarios ($\mu_0 = 0.28 \sim 0.33$). The maximum horizontal stress gradient is 10 kPa/m.

Because the initial stress and friction parameters are prescribed, the runaway potential of each fault (equation 7) is determined only by its orientation (i.e., μ_i) and the value of $\mu_f (= \mu_0 + (a - b) \log(V_p/V_0))$. In general, we find that the mainshock tends to occur earlier and reach a larger magnitude at lower μ_0 (equivalently, μ_f) and a smaller stress angle (Fig. 11). Most of the M_w >5 mainshocks occur within 10 yr, except the high θ case with a stress angle of 77.5° (Fig. 11d). The maximum magnitude is typically larger than 5 if the initial runaway potential is large (i.e., μ_0 is small). The maximum magnitude is abruptly reduced at a particular point of μ_0. For example, in the case $\theta_i = 10^{12}$ s and maximum stress orientation 80°, this happens between $\mu_0 = 0.31$ and 0.32 (Fig. 11b). This is because the mainshock fault rupture was not triggered. In all cases, earthquakes nucleate near the injector and propagate southwestward (Fig. 12). This process corresponds to the actual sequence of the 2012 Prague earthquake. If the μ_0 is low, rupture propagates down to the southwest mainshock fault (Fig. 12a,b). If the μ_0 is high, the initial rupture is arrested before it reaches the southwest mainshock fault (Fig. 12c), making the earthquake magnitude significantly lower. This is why the maximum magnitude is significantly smaller in the mainshock non-triggered cases (i.e., X-marked cases in Fig. 11a,b). If the potential for runaway rupture is very high, the rupture also propagates toward the northeast fault (Fig. 12a), which did not happen in the actual Prague sequence.

In the actual Prague earthquake sequence, the mainshock occurred ~1 day after the M_w 5.0 foreshock. We find that this time lag can result if the foreshock rupture is arrested before but close to the mainshock fault (i.e., somewhere between Fig. 12b and 12c). In this case, the mainshock is triggered after a delay due to its own nucleation time. One of our simulation sets could reproduce this delayed triggering. When the initial rupture is arrested near the mainshock fault (Fig. 13b), the mainshock fault ruptures after a day of nucleation period (Fig. 13c). To check if this occurs in the other simulation set, we conducted extra simulations in between the Fig. 12b and 12c cases. We found $\mu_0 = 0.3155$ results in the ~1-day delay between foreshock and aftershock (Fig. 13d–f). Interestingly, those delayed mainshocks propagate back into the foreshock fault, making the fault re-ruptured (Fig. 13c,f).

Our simulations could not reproduce the M_w 5 aftershock (Fig. 10b; green fault). The reason is twofold: (1) the initial runaway potential on the fault that produced this aftershock is too low due to its nonoptimal orientation, and (2) the Coulomb

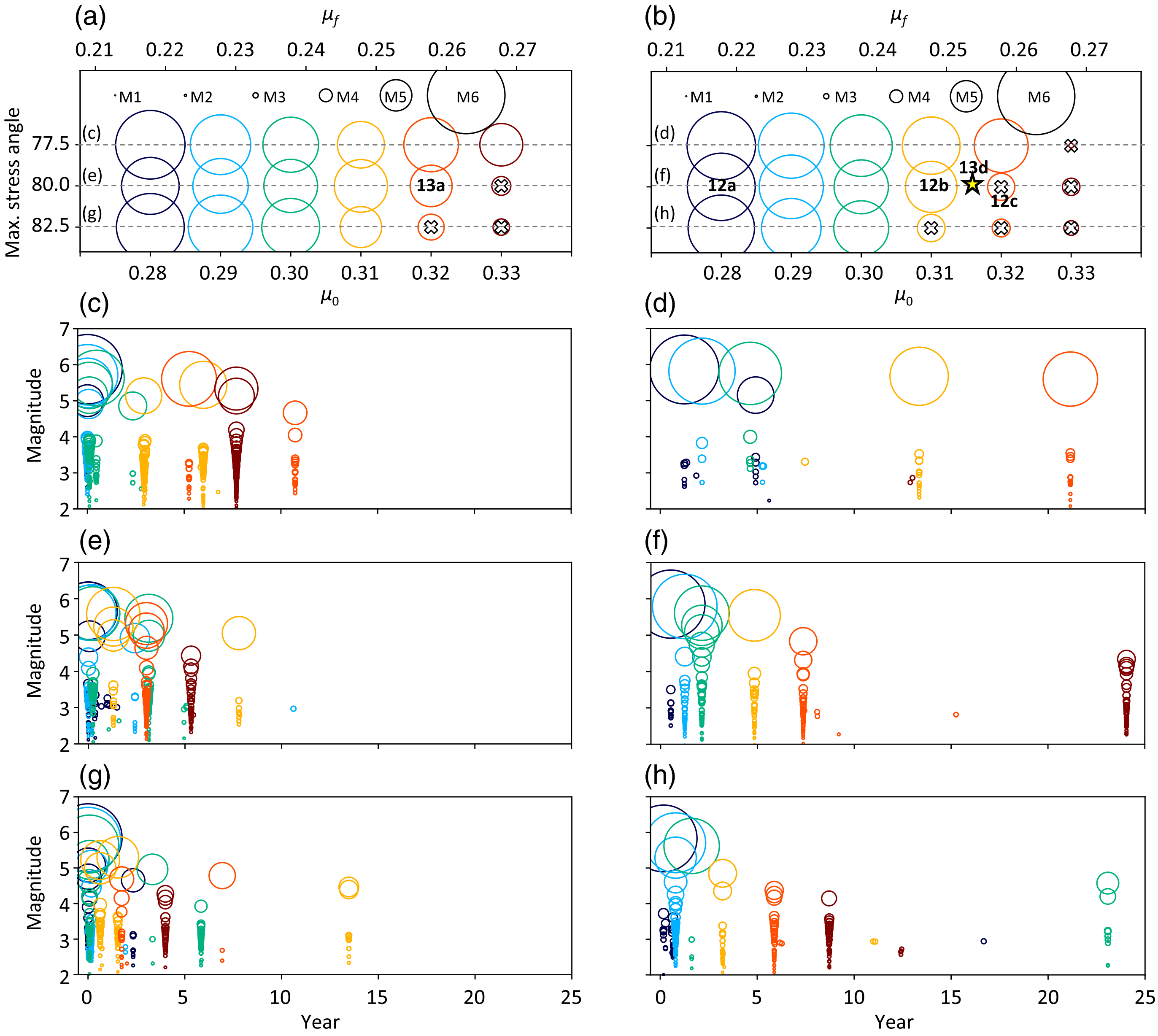

Figure 11. Simulation results for the Wizetta fault system. (a,b) Maximum earthquake magnitude within 25 yr with $\theta_i = 10^{10}$ s (~300 yr; panel (a)) and $\theta_i = 10^{12}$ s (~30,000 yr; panel (b)). The X marks denote that the mainshock fault of the Prague earthquake (i.e., the red fault in Fig. 9b) did not rupture. (c–h) Time series of induced earthquakes. The color version of this figure is available only in the electronic edition.

stress on the aftershock fault decreases during the foreshock and mainshock sequences. This is in line with the Coulomb stress analysis conducted in a previous study (Sumy *et al.*, 2014). This particular aftershock cannot be solely attributed to fault interaction in a system of faults with the same friction properties and submitted to the same stress tensor. Some other factor is needed to explain the occurrence of this event (e.g., local stress heterogeneities or a lower dynamic friction μ_f on that particular fault).

DISCUSSION

The aforementioned comparison studies are satisfying, and the application examples demonstrate that Quake-DFN can be used to simulate real-case examples of induced seismicity due to its computational efficiency. All the simulations presented in this study were calculated on a standard desktop computer (CPU: i9-13900k), and calculation times for each simulation range were <10 min (branch fault simulation in the Injection-Induced Earthquakes on a Branching Fault Systems section; 3741 elements), 15–20 min (Prague earthquake in the A Realistic Case Example: The Prague, Oklahoma, Earthquake Sequence section; 6220 elements), and 1.5–2 hr (planar fault simulations in the Injection-Induced Earthquakes on a Planar Fault section; 20,200 elements). The simulation speed with a large element

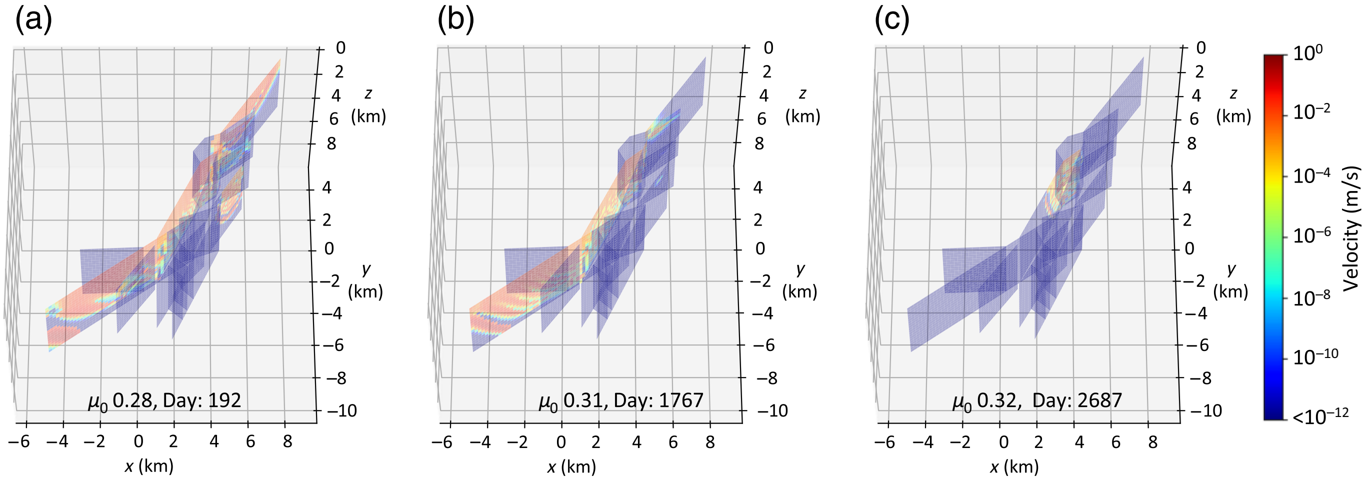

Figure 12. Snapshots of induced earthquakes with different initial setting. The parameter set for each simulation (a)–(c) is presented in Figure 11b. The color version of this figure is available only in the electronic edition.

size can be further improved using H-matrix approximation (Borm *et al.*, 2003) in the future.

In the simulations presented in the Injection-Induced Earthquakes on a Planar Fault, Injection-Induced Earthquakes on a Branching Fault Systems, and A Realistic Case Example: The Prague, Oklahoma, Earthquake Sequence sections, the normal stress is depth-dependent (Fig. 2d–f). In this case, the critical stiffness for each element is also depth-dependent, so the critical length decreases with depth, allowing localized smaller earthquakes in deeper areas. As a result, the deeper part of our fault models may contain under-resolved, inherently discrete elements, in which fault ruptures can occur at a single element. For instance, for the planar fault case ($D_c = 200$ μm and normal stress gradient 7 kPa/m), assuming $\gamma = 1$, L_c (equation 5) becomes smaller than our minimum element length (50 m) at a depth >3.8 km. This is deeper than the injection depth of 2.5 km. The simulation is well resolved near the injector, but single-element ruptures are allowed in the deeper area. This is the major source of the small aftershocks in our simulation (small earthquakes in Figs. 6 and 11). We kept the deeper area under-resolved here to limit computational time. However, users can choose to avoid this issue by adjusting grid size, normal stress, or friction parameters in deep areas because Quake-DFN does not have restrictions on the element size.

The simulations presented in this study are restricted to strike-slip motion. The code also allows dip-slip motion. It can be expanded in the future to allow for a mixed mode using two shear stiffness matrices. In this case, the rake direction should be calculated at each timestep according to the maximum stress orientation.

The simulation of induced earthquakes does not require including tectonic loading (Dieterich *et al.*, 2015), which is not necessary to simulate a sequence driven by tectonic stresses over a short period of time (short with respect to the return period of the largest event in the region of interest) (Im and Avouac, 2023). However, to simulate earthquake sequences driven by tectonics over a longer period of time, tectonic loading would need to be included. Using the current implementation of Quake-DFN, the long-term loading of a network of nonplanar faults would result in a rapid buildup of elastic stresses at the fault tips and fault kinks. In nature, stress buildup would be limited by the yielding of the bulk material surrounding the faults. A backslip approach could be adopted to address this issue cost-effectively, as done in RSQSim (Richards-Dinger and Dieterich, 2012) or MCQSim (Zielke and Mai, 2023). Another approach would be to take off-fault deformation into account (e.g., Okubo *et al.*, 2020), but that would come at an additional computational cost. Simulation of tectonically loaded faults should also, in principle, take into account postseismic processes. Quake-DFN naturally produces afterslips on rate-strengthening or conditionally stable faults but would not account for viscoelastic postseismic relaxation. Viscoelastic relaxation is generally observed after M_w >7 events and can significantly impact the spatiotemporal distribution of seismicity (e.g., Pollitz and Sacks, 2002). ViscoSim (Pollitz, 2012) was developed specifically to address that issue. It might be possible to include the effect of viscoelastic relaxation in Quake-DFN by modulating tectonic loading following the approach adopted in MCQSim.

In the simulations presented in this study, we used an analytical solution to represent the poroelastic stress change from the injection. Although this approximation could produce a realistic earthquake sequence, correctly defining pressure diffusion is another important ingredient for injection-induced earthquake forecast. A more realistic model could be used because our simulator is ready for coupling stress change calculated from external geomechanical models, for example, the Tough-FLAC coupled simulator (e.g., Rutqvist *et al.*, 2002; Taron *et al.*, 2009; Im *et al.*, 2021) as an input parameter of τ^E and σ^E in equation (1). This is a one-way coupling, but, eventually, a fully coupled earthquake simulation

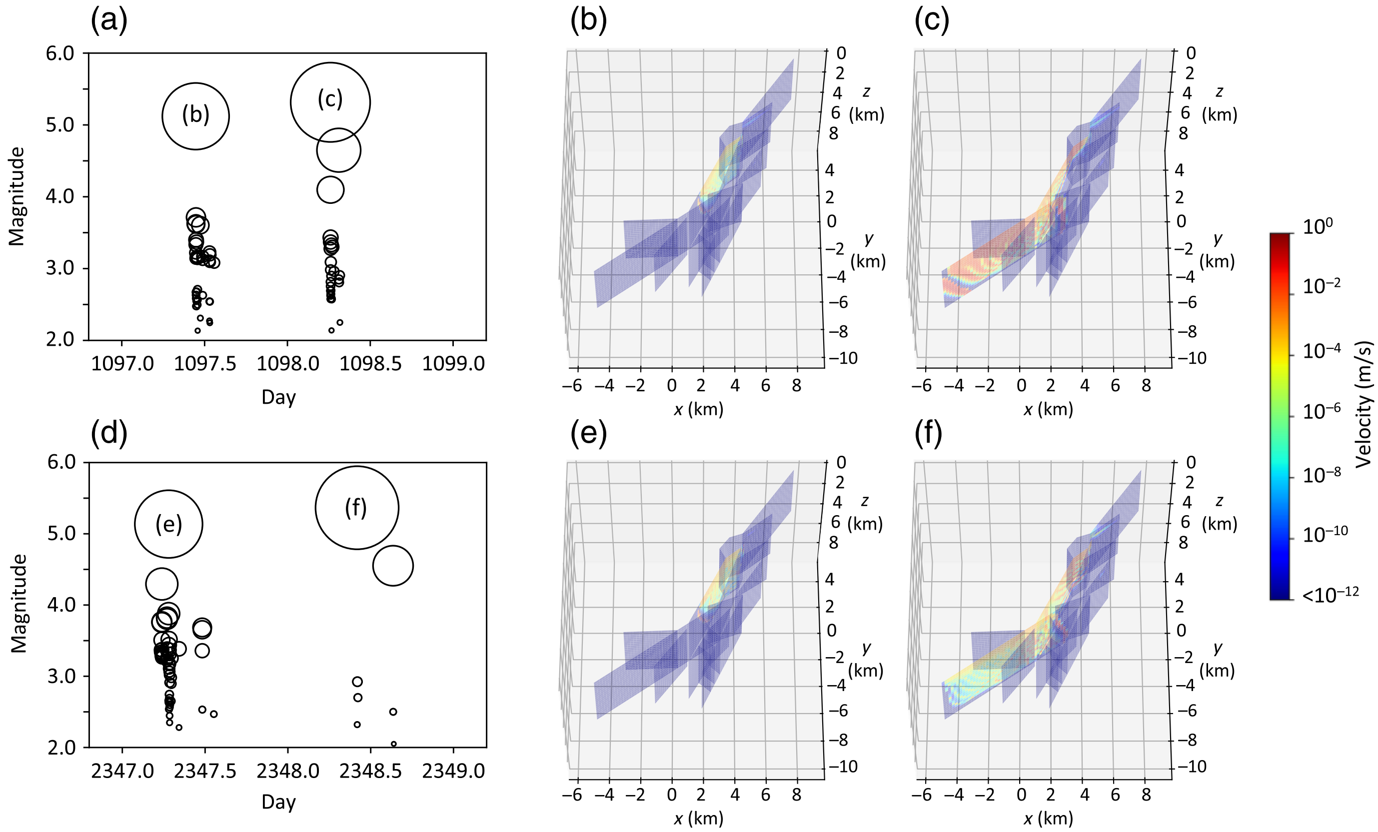

would be necessary to accommodate the permeability change that can result from fault reactivation (e.g., Guglielmi *et al.*, 2015; Im *et al.*, 2018).

Our simulation (see the Injection-Induced Earthquakes on a Planar Fault and Injection-Induced Earthquakes on a Branching Fault Systems sections) shows that larger induced earthquakes occur earlier if the runaway potential, $\mu_i - \mu_f$ (equation 7 or 8), is high. This quantity captures the effect of the initial stress on induced ruptures observed in numerical studies (Garagash and Germanovich, 2012; Dieterich *et al.*, 2015; Larochelle *et al.*, 2021). This quantity also determines the variation of coseismic slip measured along a fault with varying orientations (Milliner *et al.*, 2022). Each parameter entering this quantity can be estimated based on the local stress field and fault orientation (μ_i) or derived from laboratory friction measurements ($\mu_f = \mu_0 - (a - b)\ \log(V_0)$). Given the importance of rupture timing and magnitude, our simulation confirms that this value should be primarily considered to assess the risk of injection-induced earthquakes.

Some of the parameters entering our simulations are, in principle, measurable or inferred from laboratory studies. However, due to the uncertainty of the measurement and the heterogeneity in actual fault systems (e.g., Cattania and Segall 2021), it may be more practical to explore a wide range of parameter space to select possible sets of parameters and initial conditions. Such an approach for seismic hazard assessment would be possible with the simulator presented in his study, given its low computational cost.

Figure 13. Simulated 1-day delayed rupture. The parameter set for each simulation is presented in Figure 11a,b. (a,d) Seismicity plot of foreshock and mainshock. (b,e) Snapshots of foreshocks. (c,f) Snapshots of delayed mainshocks. The color version of this figure is available only in the electronic edition.

CONCLUSION

This study presents an earthquake simulator consistent with more advanced simulations of seismic ruptures while allowing for numerically efficient simulations of induced earthquake sequences. We, therefore, believe that the tool will be useful to gain insight into the factors controlling the time and magnitude of induced earthquakes. Some limitations of the current version of Quake-DFN can be addressed in future work, for example, by allowing for a variable rake angle or by facilitating the representation of nonplanar fault using a triangular mesh. Further improvements would be needed to allow simulations of earthquake sequences driven by tectonic loading only.

DATA AND RESOURCES

All simulation results in this article are generated by Quake-DFN. The simulator and source code are provided on GitHub (https://github.com/limkjae/Quake-DFN) and the Geomechanics and Mitigation of Geohazards (GMG) center web page (https://gmg.caltech.edu). Both websites were last accessed in May 2024. The supplemental material includes one figure (Fig. S1) and one text (Text S1), discussing the influence of the α value in equation (3). Simulation results with varied α values are shown in Figure S1 and discussed in Text S1.

DECLARATION OF COMPETING INTERESTS

The authors acknowledge that there are no conflicts of interest recorded.

ACKNOWLEDGMENTS

The authors thank Associate Editor Arben Pitarka and an anonymous reviewer for their insightful and constructive evaluations. This study was supported by the National Science Foundation (Award Number 1822214) via the Industry-University Cooperative Research (ICUR) Center for Geomechanics and Mitigation of Geohazards.

REFERENCES

Acosta, M., J. Avouac, J. D. Smith, K. Sirorattanakul, H. Kaveh, and S. J. Bourne (2023). Earthquake nucleation characteristics revealed by seismicity response to seasonal stress variations induced by gas production at Groningen, *Geophys. Res. Lett.* **50,** e2023GL105455, doi: 10.1029/2023GL105455.

Alghannam, M., and R. Juanes (2020). Understanding rate effects in injection-induced earthquakes, *Nat. Commun.* **11,** no. 1, 3053.

Barbot, S. (2019). Slow-slip, slow earthquakes, period-two cycles, full and partial ruptures, and deterministic chaos in a single asperity fault, *Tectonophysics* **768,** 228171.

Ben-Zion, Y. (1996). Stress, slip, and earthquakes in models of complex single-fault systems incorporating brittle and creep deformations, *J. Geophys. Res.* **101,** 5677–5706.

Bhattacharya, P., and R. C. Viesca (2019). Fluid-induced aseismic fault slip outpaces pore-fluid migration, *Science* **364,** 464–468.

Borm, S., L. Grasedyck, and W. Hackbusch (2003). Introduction to hierarchical matrices with applications, *Eng. Anal. Bound. Elem.* **5,** 405–422.

Bourne, S. J., and S. J. Oates (2017). Extreme threshold failures within a heterogeneous elastic thin sheet and the spatial-temporal development of induced seismicity within the Groningen gas field, *J. Geophys. Res.* **122,** 10–299.

Candela, T., C. G. Machado, O. Leeuwenburgh, and J. T. Heege (2022). A physics-informed optimization workflow to manage injection while constraining induced seismicity: The Oklahoma case, *Front. Earth Sci.* **10,** 1053951.

Candela, T., B. Wassing, J. T. Heege, and L. Buijze (2018). How earthquakes are induced. *Science* **360,** 598–600.

Cappa, F., Y. Guglielmi, and L. D. Barros (2022). Transient evolution of permeability and friction in a slowly slipping fault activated by fluid pressurization, *Nat. Commun.* **13,** 3039.

Cappa, F., M. M. Scuderi, C. Collettini, Y. Guglielmi, and J.-P. Avouac (2019). Stabilization of fault slip by fluid injection in the laboratory and in situ, *Sci. Adv.* **5,** doi: 10.1126/sciadv.aau4065.

Cattania, C., and P. Segall (2021). Precursory slow slip and foreshocks on rough faults, *J. Geophys. Res.* **126,** e2020JB020430, doi: 10.1029/2020JB020430.

Dieterich, J. H. (1979). Modeling of rock friction: 1. Experimental results and constitutive equations, *J. Geophys. Res.* **84,** 2161–2168.

Dieterich, J. H., K. B. Richards-Dinger, and K. A. Kroll (2015). Modeling injection-induced seismicity with the physics-based earthquake simulator RSQSim, *Seismol. Res. Lett.* **86,** 1102–1109.

Ellsworth, W. L. (2013). Injection-induced earthquakes, *Science* **341,** doi: 10.1126/science.1225942.

Erickson, B. A., J. Jiang, M. Barall, N. Lapusta, E. M. Dunham, R. Harris, L. S. Abrahams, K. L. Allison, J. P. Ampuero, S. Barbot, *et al.* (2020). The community code verification exercise for simulating sequences of earthquakes and aseismic slip (SEAS), *Seismol. Res. Lett.* **91,** 874–890.

Erickson, B. A., J. Jiang, V. Lambert, S. D. Barbot, M. Abdelmeguid, M. Almquist, J. P. Ampuero, R. Ando, C. Cattania, A. Chen, *et al.* (2023). Incorporating full elastodynamic effects and dipping fault geometries in community code verification exercises for simulations of earthquake sequences and aseismic slip (SEAS), *Bull. Seismol. Soc. Am.* **113,** 499–523.

Galis, M., J. P. Ampuero, P. M. Mai, and F. Cappa (2017). Induced seismicity provides insight into why earthquake ruptures stop, *Sci. Adv.* **3,** doi: 10.1126/sciadv.aap7528.

Garagash, D. I., and L. N. Germanovich (2012). Nucleation and arrest of dynamic slip on a pressurized fault, *J. Geophys. Res.* **117,** doi: 10.1029/2012JB009209.

Goebel, T. H. W., and E. E. Brodsky (2018). The spatial footprint of injection wells in a global compilation of induced earthquake sequences, *Science* **361,** 899–904, doi: 10.1126/science.aat5449.

Guglielmi, Y., F. Cappa, J.-P. Avouac, P. Henry, and D. Elsworth (2015). Seismicity triggered by fluid injection-induced aseismic slip, *Science* **348,** 1224–1226, doi: 10.1126/science.aab0476.

Hager, B. H., J. Dieterich, C. Frohlich, R. Juanes, S. Mantica, J. H. Shaw, F. Bottazzi, F. Caresani, D. Castineira, A. Cominelli, *et al.* (2021). A process-based approach to understanding and managing triggered seismicity, *Nature* **595,** 684–689.

Harris, R. A., M. Barall, B. Aagaard, S. Ma, D. Roten, K. Olsen, B. Duan, D. Liu, B. Luo, K. Bai, *et al.* (2018). A suite of exercises for verifying dynamic earthquake rupture codes, *Seismol. Res. Lett.* **89,** 1146–1162.

Harris, R. A., M. Barall, R. Archuleta, E. Dunham, B. Aagaard, J. P. Ampuero, H. Bhat, V. Cruz-Atienza, L. Dalguer, P. Dawson, *et al.* (2009). The SCEC/USGS dynamic earthquake rupture code verification exercise, *Seismol. Res. Lett.* **80,** 119–126.

Im, K., and J.-P. Avouac (2021a). On the role of thermal stress and fluid pressure in triggering seismic and aseismic faulting at the Brawley Geothermal Field, California, *Geothermics* **97,** 102238, doi: 10.1016/j.geothermics.2021.102238.

Im, K., and J.-P. Avouac (2021b). Tectonic tremor as friction-induced inertial vibration, *Earth Planet. Sci. Lett.* **576,** 117238, doi: 10.1016/j.epsl.2021.117238.

Im, K., and J.-P. Avouac (2023). Cascading foreshocks, aftershocks and earthquake swarms in a discrete fault network, *Geophys. J. Int.* **235,** 831–852.

Im, K., J.-P. Avouac, E. R. eimisson, and D. Elsworth (2021). Ridgecrest aftershocks at Coso suppressed by thermal destressing, *Nature* **595,** 70–74.

Im, K., D. Elsworth, and Y. Fang (2018). The influence of Preslip sealing on the permeability evolution of fractures and faults, *Geophys. Res. Lett.* **45,** doi: 10.1002/2017GL076216.

Im, K., D. Elsworth, C. Marone, and J. Leeman (2017). The impact of frictional healing on stick-slip recurrence interval and stress drop: Implications for earthquake scaling, *J. Geophys. Res.* doi: 10.1002/2017JB014476.

Jiang, J., B. A. Erickson, V. R. Lambert, J. P. Ampuero, R. Ando, S. D. Barbot, C. Cattania, L. D. Zilio, B. Duan, E. M. Dunham, *et al.* (2022).

Community-driven code comparisons for three-dimensional dynamic modeling of sequences of earthquakes and aseismic slip, *J. Geophys. Res.* **127,** e2021JB023519, doi: 10.1029/2021JB023519.

Keranen, K. M., H. M. Savage, G. A. Abers, and E. S. Cochran (2013). Potentially induced earthquakes in Oklahoma, USA: Links between wastewater injection and the 2011 Mw 5.7 earthquake sequence, *Geology* **41,** 699–702.

Kroll, K. A., J. H. Dieterich, K. B. Richards-Dinger, and D. D. Oglesby (2023). 3-D Simulations of earthquakes rupture jumps: 1. Homogeneous pre-stress conditions, *Geophys. J. Int.* **234,** 395–403.

Langenbruch, C., and M. D. Zoback (2016). How will induced seismicity in Oklahoma respond to decreased saltwater injection rates? *Sci. Adv.* **2,** e1601542, doi: 10.1126/sciadv.1601542.

Lapusta, N., J. R. Rice, Y. Ben-Zion, and G. Zheng (2000). Elastodynamic analysis for slow tectonic loading with spontaneous rupture episodes on faults with rate-and state-dependent friction, *J. Geophys. Res.* **105,** 23,765–23,789.

Larochelle, S., N. Lapusta, J. Ampuero, and F. Cappa (2021). Constraining fault friction and stability with fluid-injection field experiments, *Geophys. Res. Lett.* **48,** e2020GL091188, doi: 10.1029/2020gl091188.

Lee, K. K., W. L. Ellsworth, D. Giardini, J. Townend, S. Ge, T. Shimamoto, I. W. Yeo, T. S. Kang, J. Rhie, D. H. Sheen, *et al.* (2019). Managing injection-induced seismic risks, *Science* **364,** 730–732.

Linker, M. F., and J. H. Dieterich (1992). Effects of variable normal stress on rock friction: Observations and constitutive equations, *J. Geophys. Res.* **97,** no. B4, 4923, doi: 10.1029/92JB00017.

Madariaga, R. (1976). Dynamics of an expanding circular fault, *Bull. Seismol. Soc. Am.* **66,** 639–666.

Marone, C. (1998). Laboratory-derived friction laws and their application to seismic faulting, *Annu. Rev. Earth Planet. Sci.* **26,** 643–696, doi: 10.1146/annurev.earth.26.1.643.

McGarr, A. (2014). Maximum magnitude earthquakes induced by fluid injection, *J. Geophys. Res.* **119,** 1008–1019.

Milliner, C. W. D., S. Aati, and J.-P. Avouac (2022). Fault friction derived from fault bend influence on coseismic slip during the 2019 Ridgecrest Mw 7.1 mainshock, *J. Geophys. Res.* **127,** e2022JB024519, doi: 10.1029/2022JB024519.

Norbeck, J. H., and J. L. Rubinstein (2018). Hydromechanical earthquake nucleation model forecasts onset, peak, and falling rates of induced seismicity in Oklahoma and Kansas, *Geophys. Res. Lett.* **45,** 2963–2975.

Okada, Y. (1992). Internal deformation due to shear and tensile faults in a half-space, *Bull. Seismol. Soc. Am.* **82,** 1018–1040.

Okubo, K., E. Rougier, Z. Lei, and H. S. Bhat (2020). Modeling earthquakes with off-fault damage using the combined finite-discrete element method, *Comput. Part. Mech.* **7,** 1057–1072.

Olsen, K. B., R. Madariaga, and R. J. Archuleta (1997). Three-dimensional dynamic simulation of the 1992 Landers earthquake, *Science* **278,** 834–838.

Pollitz, F. F. (2012). ViscoSim earthquake simulator, *Seismol. Res. Lett.* **83,** 979–982

Pollitz, F. F., and I. S. Sacks (2002). Stress triggering of the 1999 Hector Mine earthquake by transient deformation following the 1992 Landers earthquake, *Bull. Seismol. Soc. Am.* **92,** 1487–1496.

Rice, J. R. (1993). Spatio-temporal complexity of slip on a fault, *J. Geophys. Res.* **98,** 9885, doi: 10.1029/93JB00191.

Richards-Dinger, K., and J. H. Dieterich (2012). RSQSim earthquake simulator, *Seismol. Res. Lett.* **83,** no. 6, 983–990.

Rudnicki, J. W. (1986). Fluid mass sources and point forces in linear elastic diffusive solids, *Mech. Mater.* **5,** 383–393.

Rutqvist, J., Y.-S. Wu, C.-F. Tsang, and G. Bodvarsson (2002). A modeling approach for analysis of coupled multiphase fluid flow, heat transfer, and deformation in fractured porous rock, *Int. J. Rock Mech. Min. Sci.* **39,** 429–442, doi: 10.1016/S1365-1609(02)00022-9.

Sáez, A., and B. Lecampion (2024). Fluid-driven slow slip and earthquake nucleation on a slip-weakening circular fault, *J. Mech. Phys. Solids* **183,** 105506, doi: 10.1016/j.jmps.2023.105506.

Segall, P., and S. Lu (2015). Injection-induced seismicity: Poroelastic and earthquake nucleation effects, *J. Geophys. Res.* **120,** 5082–5103.

Shaw, B. E., K. R. Milner, E. H. Field, K. Richards-Dinger, J. J. Gilchrist, J. H. Dieterich, and T. H. Jordan (2018). A physics-based earthquake simulator replicates seismic hazard statistics across California, *Sci. Adv.* **4,** eaau0688, doi: 10.1126/sciadv.aau0688.

Sumy, D. F., E. S. Cochran, K. M. Keranen, M. Wei, and G. A. Abers (2014). Observations of static Coulomb stress triggering of the November 2011 M5.7 Oklahoma earthquake sequence, *J. Geophys. Res.* **119,** 1904–1923, doi: 10.1002/2013JB010612.

Taron, J., D. Elsworth, and K.-B. Min (2009). Numerical simulation of thermal-hydrologic-mechanical-chemical processes in deformable, fractured porous media, *Int. J. Rock Mech. Min. Sci.* **46,** 842–854, doi: 10.1016/j.ijrmms.2009.01.008.

Thomas, M. Y., N. Lapusta, H. Noda, and J. Avouac (2014). Quasi-dynamic versus fully dynamic simulations of earthquakes and aseismic slip with and without enhanced coseismic weakening, *J. Geophys. Res.* **119,** 1986–2004.

Viesca, R. C., and D. I. Garagash (2018). Numerical methods for coupled fracture problems, *J. Mech. Phys. Solids* **113,** 13–34.

Wang, T. A., and E. M. Dunham (2022). Hindcasting injection-induced aseismic slip and microseismicity at the Cooper Basin Enhanced Geothermal Systems Project, *Sci. Rep.* **12,** 19481.

Zhai, G., M. Shirzaei, and M. Manga (2020). Elevated seismic hazard in Kansas due to high-volume injections in Oklahoma, *Geophys. Res. Lett.* **47,** e2019GL085705, doi: 10.1029/2019GL085705.

Zielke, O., and P. M. Mai (2023). MCQsim: A multicycle earthquake simulator, *Bull. Seismol. Soc. Am.* **113,** 889–908.

Zoback, M. D., and S. M. Gorelick (2012). Earthquake triggering and large-scale geologic storage of carbon dioxide, *Proc. Natl. Acad. Sci.* **109,** no. 26, 10164–10168.

Manuscript received 4 December 2023
Published online 31 May 2024